

# **The interaction between p53 and Mdm2 is independent of MEG3–p53 association**

Nicholas C. Bauer<sup>a</sup>, Anli Yang<sup>b,†,§</sup>, Xin Wang<sup>b,†,||</sup>, Yunli Zhou<sup>b</sup>, Anne Klibanski<sup>b,‡,¶</sup>, Roy J. Soberman<sup>a,\*;‡</sup>

<sup>a</sup> Division of Nephrology, Department of Medicine, Massachusetts General Hospital and Harvard Medical School, Charlestown, MA 02129

<sup>b</sup> Neuroendocrine Unit, Department of Medicine, Massachusetts General Hospital and Harvard Medical School, Boston, MA 02114

\* To whom correspondence should be addressed. Tel: +1 617-455-2003; Email:

[soberman@helix.mgh.harvard.edu](mailto:soberman@helix.mgh.harvard.edu)

† These authors contributed equally to the work

‡ These authors contributed equally to the work

§ Current affiliation: Department of Histology and Embryology, Guangdong Pharmaceutical University, Guangzhou, Guangdong, China

|| Current affiliation: Department of Breast Oncology, Sun Yat-sen University Cancer Center, Guangzhou, Guangdong, China

¶ Current affiliation: Partners Healthcare, Somerville, MA

## ABSTRACT

The ability of the long noncoding RNA MEG3 to suppress cell proliferation led to its recognition as a tumor suppressor. MEG3 has previously been shown to bind to p53 in vitro, which led us to hypothesize that MEG3 functions by disrupting the interaction of p53 and its E3 ubiquitin ligase Mdm2. To test this hypothesis in vivo, we built a cross-nearest neighbor/Monte Carlo analytical method based on two color direct stochastic optical reconstruction microscopy (dSTORM), a single-molecule localization microscopy (SMLM) technique. Our data support the interaction of MEG3 and p53. Surprisingly, this association had no effect on the binding of p53 and Mdm2, distinct from the most commonly proposed model for the mechanism of MEG3 action. Additionally, our mathematical approach to analyzing SMLM data has general applicability to assessing molecular interactions in a native cellular context.

## INTRODUCTION

The mechanisms by which long noncoding RNAs (lncRNAs) play multiple roles in cellular function are still not well understood. The human *MEG3* lncRNA gene is located on chromosome 14q32 and belongs to the conserved, imprinted *DLK1-MEG3* locus (Naoki *et al.*, 2000; Zhang *et al.*, 2003) that plays an important role in mammalian growth and development (Takahashi *et al.*, 2009; Takahashi *et al.*, 2010; Das *et al.*, 2015). MEG3 transcripts are detected in a wide range of normal tissues, including endocrine tissues, brain, gonads, and placenta (Zhang *et al.*, 2003). More recently MEG3 has been shown to modulate the activity of multiple miRNAs; for example, MEG3 functions as a decoy for miR-138 (Li *et al.*, 2018) allowing it to regulate the generation of IL-1 $\beta$  in macrophages in models of host defense. MEG3 has also been reported to directly interact with DNA to modulate the transcription of TGF- $\beta$  pathway genes (Mondal *et al.*, 2015).

Based on the observation that *MEG3* expression is lost in clinically non-functioning pituitary adenomas, we identified *MEG3* as a tumor suppressor (Zhang *et al.*, 2003; Zhao *et al.*, 2005;

Gejman *et al.*, 2008; Cheunsuchon *et al.*, 2011). Compared to normal tissue, MEG3 expression is also significantly reduced or absent in hepatocellular carcinomas (Braconi *et al.*, 2011), meningiomas (Zhang *et al.*, 2010), gliomas (Wang *et al.*, 2012), gastric cancer (Yan *et al.*, 2014), epithelial ovarian cancer (Sheng *et al.*, 2014), and squamous cell carcinoma of the tongue (Jia *et al.*, 2014); supporting its role as a tumor suppressor. This function was further supported by studies of tumor xenograft growth in nude mice (Wang *et al.*, 2012; Lu *et al.*, 2013; Qu *et al.*, 2013). Several studies demonstrated that MEG3 expression causes an increase in Cellular tumor antigen p53 (p53, UniprotKB P04637) levels and selectively activates p53 target gene expression (Linares *et al.*, 2003; Zhou *et al.*, 2007; Huang *et al.*, 2011; Lu *et al.*, 2013; Sun *et al.*, 2014), suggesting that MEG3 functions via p53. However, how the MEG3 lncRNA activates p53 remains elusive.

The mechanisms by which MEG3 and other lncRNAs function on a cellular basis are complex, and different mechanisms can occur simultaneously within one cell. Our previous work indicated that MEG3 functions via activation of tumor suppressor p53 (Zhou *et al.*, 2007). A transcription factor, p53 coordinates a transcription program to stall the cell cycle, promote DNA repair, and initiate senescence or apoptosis (Ryan *et al.*, 2001). The primary modulators of p53 activity are E3 ubiquitin-protein ligase Mdm2 (Mdm2, UniprotKB Q00997) and its heterodimer partner Protein Mdm4 (Mdm4, UniprotKB O1515) which constitutively polyubiquitinate p53 for proteasomal degradation, maintaining p53 at low levels (Gu *et al.*, 2002; Toledo and Wahl, 2006; Perry, 2010). Thus, modulating the p53–Mdm2/4 interaction is a critical point of regulation for p53 activity. Signal-dependent post-translational modification of p53, including phosphorylation and acetylation, can block Mdm2/4 from binding to p53 and prevent its degradation (Bauer *et al.*, 2015). Stabilization of p53 may also be achieved through interaction with other proteins such as Peptidyl-prolyl cis-trans isomerase NIMA-interacting 1 (Pin1) (Zacchi *et al.*, 2002; Zheng *et al.*, 2002). It has been shown that MEG3 and p53 can be pulled down in one complex by immunoprecipitation

(Zhu *et al.*, 2015; Yan *et al.*, 2016). Therefore, one possible mechanism for p53 activation by MEG3 is disrupting the p53–Mdm2/4 interaction.

To test the hypothesis that MEG3 disrupts p53–Mdm2 binding, we employed direct stochastic optical reconstruction microscopy (dSTORM) single molecule localization microscopy (SMLM) to record the precise positions of MEG3, p53, and Mdm2 in vivo and developed an approach to define and quantify their relationships. The approach characterizes the p53–Mdm2 and p53–MEG3 association by a new cross-nearest neighbor/Monte Carlo algorithm. In contrast to previous models, our data support a model in which MEG3 modulates p53 independently of Mdm2.

## RESULTS

### Quantifying the associations of MEG3, p53, and Mdm2 by SMLM

The subcellular compartmentalization of lncRNAs like MEG3 is a critical determinant of their mechanism of action. As a result, identifying molecular associations within the spatial context of the cell is necessary to fully define their behaviors. SMLM is exceptionally well positioned to provide this information. SMLM is unique from other microscopy approaches in that it provides high-accuracy coordinates of the positions of fluorophores rather than an image (although an image may be reconstructed from these localizations). As such, SMLM data must be analyzed with very different methods from traditional microscopy data, which are still under active development (Feher *et al.*, 2019). To use SMLM to examine the binding of MEG3, p53, and Mdm2, we developed an approach that allowed us to identify potentially interacting molecules within cells by calculating the probability that two localizations were anomalously close. We applied a Monte Carlo estimation method that accounts for the local density around a candidate binding pair, partly based on a technique recently introduced for examining the association of sparse mRNAs in neurons (Eliscovich *et al.*, 2017). Our method is illustrated in Figure 1.

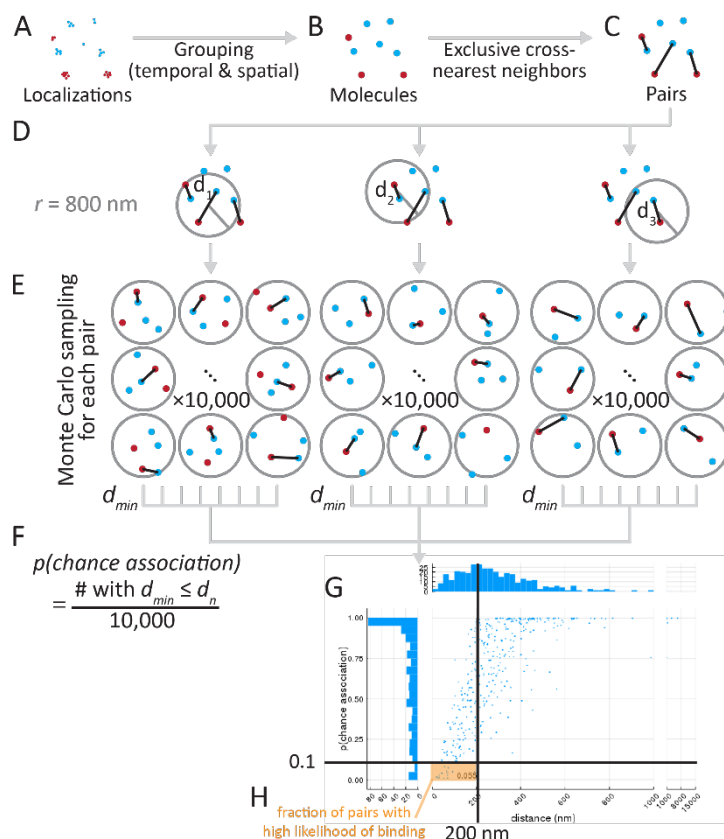


**Figure 1. Cross-nearest neighbor/Monte Carlo method to estimate fraction of molecules bound.** Scattered localizations (A) were grouped over time and space to produce “molecules” (B; see Figure S3). These molecules were exclusively paired to their cross-nearest neighbor (C). For each pair (D), 10,000 permutations of the molecules within radius  $r$  (800 nm) of the centroid of the pair were generated and the closest intermolecular distance was measured (E). The fraction of events less than the pair’s distance was the probability of chance association ( $p(\text{chance association})$ ) (F). These values were accumulated across the whole cell (plotted in G), and the fraction of pairs with a probability of chance association  $< 0.1$  and within a physically possible binding distance ( $< 200 \text{ nm}$ ), the

First, nearby localizations were grouped into “molecules” using spatial and temporal thresholds (Figure 1A, B). A characteristic of dSTORM is that there is no guarantee that a single molecule will be represented by a single localization. Consider the p53 tetramer: it may be bound by up to 4 primary single-epitope antibodies, each of which may be bound by 1 or 2 secondary antibodies, each of which may have 0-8 fluorophores attached (despite the average being  $\sim 1$  dye molecule/antibody), and each fluorophore may blink many times before permanent bleaching. A grouping algorithm is important for dSTORM data to remove such autocorrelated localizations for our downstream analysis, which here assumes that each molecule’s location is independent of each other molecule.

Second, identified molecules from each channel were paired together through an exclusive cross-nearest neighbor algorithm: closest pair identified then removed, repeating until all possible pairs were made (Figure 1B and 1C). The resulting list of pairs is guaranteed to contain all detectable binding events.

The third phase of the algorithm assesses the probability that each pair is associated by chance. Within the local neighborhood (radius  $r = 800$  nm, Figure 1D), 10,000 random permutations of the positions of the molecules within this radius were generated and the smallest paired distance measured in each iteration (Figure 1E). The fraction of permutations in which a distance  $d_n$  less than or equal to the observed distance  $d_{min}$  was recorded as the probability of chance association ( $p(\text{chance association})$ ) for that molecule pair (Figure 1F). These steps were repeated for each pair in each cell, and a graph of distance and probability of chance association may be generated (Figure 1G). This plot from a representative cell shows that larger distance is correlated with higher probability of chance association, with wide variability due to local density changes.

Finally, these pairwise measures of association were reduced into a summary figure which would correlate with fraction bound. We considered pairs with a probability of chance association less than 0.1 and a distance of less than 200 nm to be bound, and used that value to generate the final output, fraction bound (Figure 1H). In this example, the average distance of the pairs in the “bound” fraction is approximately 50 nm, which corresponds well with the range expected due to the size of the antibody stacks used to detect molecules (up to ~70 nm between fluorophores, Figure 2). In this dataset, pairs with a large distance but a low probability of chance association were rare; most of those pairs classified as unbound were due to moderately close pairs in dense areas.

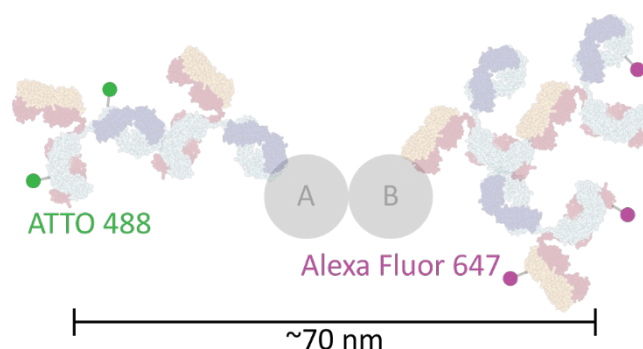


**Figure 2. Illustration of physical arrangement of a bound pair and antibody stack.** Typical immunofluorescence uses expensive, target-specific primary antibodies and cheap secondary antibodies conjugated to a fluorophore like ATTO 488 and Alexa Fluor 647. The physical size and arrangement mean that ~70 nm may separate signal from the two fluorophores when detecting a binding interaction between proteins A and B, and multiple fluorophores can produce signal spread over tens of nanometers. Antibody graphic was created using NGL Viewer (52) from RCSB PDB 1IGT.

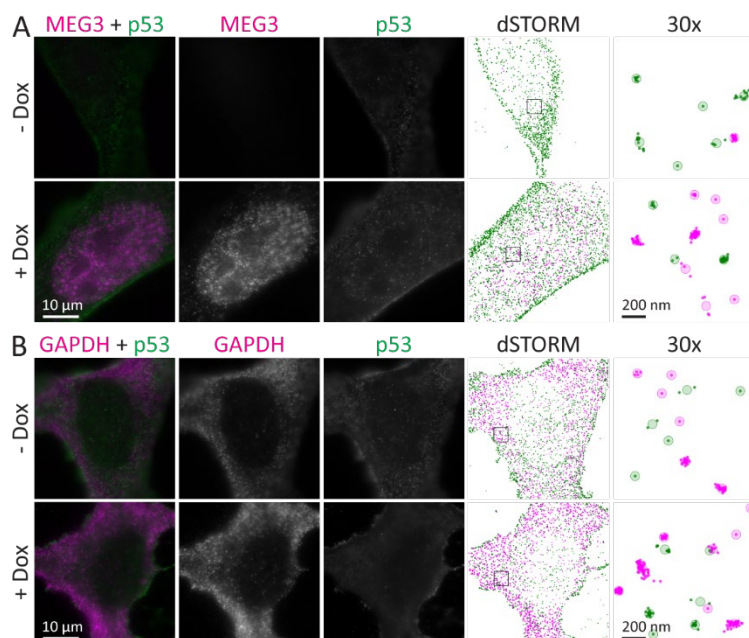


**Figure 3. Doxycycline induced MEG3 in the nucleus of U2OS cells.** MEG3 was induced by treatment of U2OS-MEG3 cells for 20 h with 1 μg/mL doxycycline. Cells were stained for p53 with a secondary antibody conjugated to ATTO 488 (green) and either tiled oligonucleotides recognizing MEG3 (Quasar 670, magenta, A) or GAPDH (Quasar 570, magenta, B). From left to right: Merged image; RNA channel; p53 channel; dSTORM localization map; 30x inset of dSTORM localizations in the black box, with shaded circles indicating “molecules”. Scale bars are 10 μm, or 200 nm (right column).

### MEG3–p53 interaction

We developed a group of U2OS osteosarcoma cell clones containing a doxycycline-inducible MEG3 (U2OS-MEG3) and confirmed that MEG3 was induced 100–200-fold on doxycycline treatment as determined by qRT-PCR. We established conditions for simultaneously imaging RNA and protein by combined fluorescence in situ hybridization (FISH) and immunofluorescence (IF) with dSTORM. After 20 h induction with doxycycline, cells were fixed and MEG3 was labeled with a tiled probe set conjugated with Quasar 670 (magenta) and p53 was labeled with a secondary antibody conjugated to ATTO 488 (green). Cells were separately labeled for *GAPDH* mRNA with a tiled probe set conjugated with Quasar 570 (magenta) as a negative control. Large tiled widefield fluorescence images were taken (Figure S1) and ten individual cells were randomly selected from these fields for dSTORM, in each of three replicates. Representative cells are shown in Figure 3, widefield (left three columns) and dSTORM localizations and grouped molecules (right two columns, respectively). The intense fluorescence indicating MEG3 is readily apparent in the nucleus of the cells treated with doxycycline, along with p53, while very little MEG3 is apparent in untreated cells (Figure 3A). Doxycycline treatment had no apparent effect on the



GAPDH mRNA distribution (Figure 3B). As seen in the detail of the molecule groups (right column), the grouping operation is slightly biased towards merging nearby clusters.

Using the new cross-nearest neighbor/Monte Carlo method, we found a stark difference between MEG3 and *GAPDH* mRNA in terms of fraction bound (Figure 4A). Two-way nested ANOVA confirmed that the binding fraction was significantly larger for MEG3 than for *GAPDH* mRNA ( $F = 19.41$ ,  $p = 0.002271$ ,  $\omega^2 = 0.3153$ ), but no significant effect due to doxycycline ( $F = 2.407$ ,  $p = 0.1594$ ,  $\omega^2 = 0.02410$ ) and no interaction effect ( $F = 2.400$ ,  $p = 0.1599$ ,  $\omega^2 = 0.02398$ ). Since only the RNA main effect was significant, a follow-up one-way nested ANOVA was performed within each RNA type. For *GAPDH* mRNA, ~4% of p53–*GAPDH* mRNA pairs were “bound”, with virtually no change due to doxycycline (-Dox: 4.26% vs. +Dox: 4.26%;  $F = 2.134 \times 10^{-5}$ ,  $p = 0.9965$ ,  $\omega^2 = -0.05834$ ) and little variability between cells overall, though significant inter-replicate variability was present ( $F = 4.448$ ,  $p = 0.003520$ ,  $\omega^2 = 0.2714$ ) (Figure 4A, right). There are several reasons why the method has measured some binding between p53 and *GAPDH* mRNA. First, p53 is known to have promiscuous non-specific RNA binding capacity

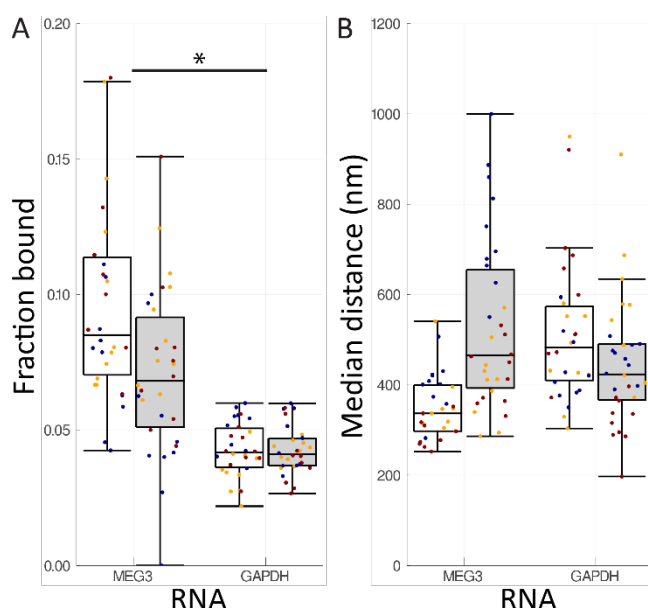


**Figure 4. MEG3 associated with p53.** MEG3 was induced by treatment of U2OS-MEG3 cells for 20 h with (gray) or without (white) 1  $\mu$ g/mL doxycycline. Cells were then fixed and stained for 2-color dSTORM of MEG3 and p53 (left) or *GAPDH* mRNA and p53 (right). For each condition, single molecule localizations were collected from 10 randomly chosen cells in 3 separate experiments. (A) Fraction of pairs bound, as defined by a probability of chance association  $< 0.1$  (i.e., correction for local density) and distance  $< 200$  nm (upper limit for binding distance, accounting for error). (B) Median distance between pairs for each cell (nm). Boxes indicate median  $\pm$  upper and lower quartile; whiskers indicate the range excluding outliers. Data points are colored by replicate. \* indicates  $p < 0.05$  by nested two-way ANOVA.



(Riley and Maher, 2007). Due to the high overall concentration of molecules in these cells, a few associations may be expected observed by chance. Another contribution may be crosstalk, due to the spectral overlap of the fluorophore used for *GAPDH* mRNA and p53 (Quasar 570 vs. ATTO 488); localizations would be associated with each other but for a technical and not biological reason. In contrast with *GAPDH* mRNA, the median fraction of MEG3 bound to p53 as defined by this method was substantially higher at ~9%, and doxycycline induction did not significantly affect this amount (-Dox: 10.21%, +Dox: 7.11%;  $F = 2.539$ ,  $p = 0.1863$ ,  $\omega^2 = 0.07640$ ) with wide variability (Figure 4A, left). No significant effect due to MEG3 induction suggests that the fraction of MEG3 bound to p53 remains constant in vivo across changes in MEG3 expression. For comparison, we also applied a naïve median distance approach, where we calculated the median of the pairwise distances for each cell (Figure 4B). In this simple approach, there is a high degree of overlap between MEG3 and *GAPDH* mRNA distributions ( $F = 0.3046$ ,  $p = 0.5961$ ,  $\omega^2 = -0.3323$ ), and increased inter-replicate variability is apparent with this measure (blue, red, orange points;  $F = 13.53$ ,  $p = 2.018 \times 10^{-13}$ ,  $\omega^2 = 0.5311$ ) (Figure 4B). Thus, our cross-nearest neighbor/Monte Carlo-based approach provides a more consistent and robust measure of association over simpler approaches.

### **MDM2–p53 binding is unaffected by MEG3 expression**

To determine whether MEG3 causes accumulation of p53 by disrupting the Mdm2–p53 interaction, MEG3 was induced in U2OS-MEG3 cells, with or without treatment with MDM2–p53 binding inhibitor nutlin-3a. After 24 h of exposure to doxycycline and/or nutlin-3a, cells were fixed. p53 was labeled with a secondary antibody conjugated to Alexa Fluor 647 (magenta) and Mdm2 was labeled with a secondary antibody conjugated to ATTO 488 (green). Large tiled widefield fluorescence images were taken (Figure S2) and ten individual cells were randomly selected from these fields for dSTORM, in each of three replicates. Representative cells are shown in Figure 5, widefield (left three columns) and dSTORM localizations and grouped molecules (right two

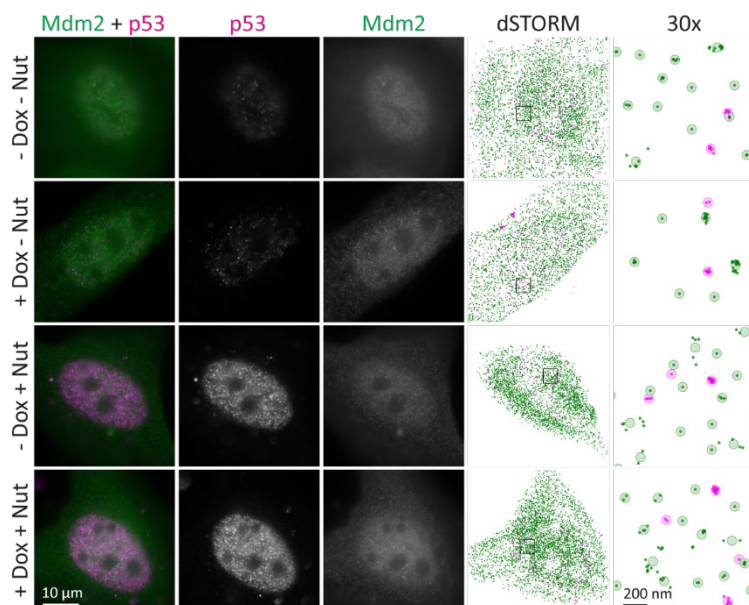


**Figure 5. Nutlin-3a caused accumulation of p53 in the nucleus.** MEG3 was induced by treatment of U2OS-MEG3 cells for 20 h with 1 μg/mL doxycycline and/or 1 μg/mL nutlin-3a. Cells were stained for Mdm2 with a secondary antibody conjugated to ATTO 488 (green) and for p53 with a secondary antibody conjugated to Alexa Fluor 647 (magenta). From left to right: Merged image; RNA channel; p53 channel; dSTORM localization map; 30x inset of dSTORM localizations in the black box, with shaded circles indicating “molecules”. Scale bars are 10 μm, or 200 nm (right column).

columns, respectively). Intense nuclear p53 fluorescence is observed on treatment with nutlin-3a, without much apparent change due to doxycycline. Apparent Mdm2 levels and localization change little between conditions. Individual cells were randomly selected from these fields for dSTORM (Figure 5).

Using the new cross-nearest neighbor/Monte Carlo method, we found that nutlin-3a treatment caused a significant decrease in p53–Mdm2 binding (-Nut: 7.32%, +Nut: 5.10%;  $F = 6.842$ ,  $p = 0.03085$ ,  $\omega^2 = 0.1210$ ) (Figure 6A). Doxycycline treatment (MEG3 induction) did not have any significant overall effect (-Dox: 5.66%, +Dox: 6.77%;  $F = 1.719$ ,  $p = 0.2262$ ,  $\omega^2 = 0.01489$ ). There was no significant interaction effect ( $F = 0.2855$ ,  $p = 0.6076$ ,  $\omega^2 = -0.01479$ ). There was significant inter-replicate variability ( $F = 3.546$ ,  $p = 0.001105$ ,  $\omega^2 = 0.1784$ ). A follow-up nested one-way ANOVA within the -Nut condition showed a moderate but low-certainty *increase* in p53–Mdm2 binding with MEG3 induction ( $F = 2.539$ ,  $p = 0.1863$ ,  $\omega^2 = 0.0764$ ). Importantly, these data demonstrate that MEG3 does not disrupt p53-Mdm2 binding. For comparison, we again conducted an analysis based on naïve median distances. As with MEG3-p53 binding, we found this simple approach produced overlapping, hard-to-interpret distributions (Figure 6B).

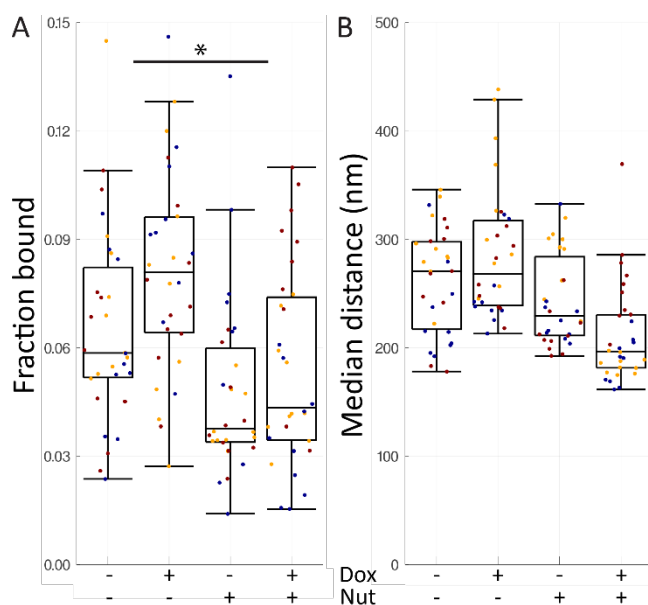


**Figure 6. Nutlin-3a, but not MEG3, reduced Mdm2-p53 binding.** MEG3 was induced by treatment of U2OS-MEG3 cells for 20 h with or without 1  $\mu$ g/mL doxycycline and/or 10  $\mu$ M nutlin-3a. Cells were then fixed and stained for 2-color dSTORM of p53 and Mdm2. For each condition, single molecule localizations were collected from 10 randomly chosen cells in 3 separate experiments. (A) Fraction of pairs bound, as defined by a probability of chance association < 0.1 (i.e., correction for local density) and distance < 200 nm (upper limit for binding distance, accounting for error). (B) Median distance between pairs for each cell (nm). Boxes indicate median +/- upper and lower quartile; whiskers indicate the range excluding outliers. Data points are colored by replicate. \* indicates  $p < 0.05$  by nested two-way ANOVA.

## DISCUSSION

We developed a technique to interrogate the interactions and mechanism of MEG3 inside the cell using SMLM. Our technique takes advantage of high-resolution molecule position data to calculate distances between putative binding partners, assesses the probability that the two molecules are not bound together, and thus provides an overall measure of the fraction of pairs of molecules likely bound together. This technique was able to distinguish between non-binding pairs (*GAPDH* mRNA-p53) and binding pairs (MEG3-p53) in vivo, and detected a robust, linear shift in fraction of Mdm2-p53 bound when a small molecule inhibitor of this interaction, nutlin-3a, was introduced. The evidence obtained through this technique is not consistent with the prior hypothesis that MEG3 acts by protecting p53 from polyubiquitination by Mdm2, as induction of MEG3 was not accompanied by a decrease in Mdm2-p53 binding. Moreover, the fraction of binding assessed between MEG3 and p53 indicates that far too few stable interactions are occurring to effectively inhibit Mdm2-p53 binding. These data suggest that MEG3 activates p53 through alternative mechanisms.

Under MEG3 induction, p53 transcription activation is selective, inducing certain targets (e.g., *GDF15*) but avoiding others (e.g., *CDKN1A*) (Zhou *et al.*, 2007). It may be that the MEG3–p53 heterodimer fails to strongly induce Mdm2 expression, thereby suppressing the negative feedback regulatory loop. MEG3 also interacts with the chromatin remodeler Polycomb repressive complex 2 (PRC2) (Zhao *et al.*, 2010; Kaneko *et al.*, 2014), which is responsible for forming heterochromatin at target sites. MEG3 targets PRC2 to certain sites via DNA triplex formation (e.g., TGF- $\beta$  pathway genes) (Mondal *et al.*, 2015) and protects other sites from PRC2 activity (e.g., *MEG3* locus) (Das *et al.*, 2015). A recent investigation of MEG3 structure identified a pseudoknot critical for p53 activation, which however was not involved in p53 binding (Uroda *et al.*, 2019). It is also possible that MEG3 may modulate the activity of Mdm2 on p53 by forming a ternary complex with them. Similar interactions have been observed with p14<sup>ARF</sup> (Tumor suppressor ARF) (Savchenko *et al.*, 2008), UCH-L1 (Ubiquitin carboxyl-terminal hydrolase isozyme L1) (Li *et al.*, 2010), and the 5S RNP (Sloan *et al.*, 2013). Future work will need to address these alternative mechanisms.

There are some important challenges to the in vivo SMLM-based binding analysis we have developed, and which affect SMLM analysis approaches in general. First, despite the 10-20 nm resolution of each localization, the large distance between the molecule of interest and the fluorophore greatly limit the analytical resolution. A typical two-antibody stack can have a displacement of up to ~35 nm from the bound epitope to the conjugated fluorophore; thus, the fluorophores for a bound pair of molecules may be separated by 70 nm or more (Figure 2), depending on the distance between epitopes. In addition, the antibody stack may be free to rotate and flex at the neck, adding variability in the position of the fluorophore during imaging (Saphire *et al.*, 2002). These distance issues may be addressed in part using F(ab)' fragments or nanobodies (small single-domain antibody fragments derived from camelids) (Carrington *et al.*, 2019; Sograte-Idrissi *et al.*, 2019) as secondary antibodies. Further distance reduction and stable

positioning could be achieved by introducing a fusion tag into the target gene and directly binding it with a labeled primary antibody or nanobody (Sograte-Idrissi *et al.*, 2019).

A second set of limitations comes from the stochastic nature of SMLM. Fluorophores may blink many times, only once, or not at all (Annibale *et al.*, 2011). This phenomenon makes it difficult to distinguish between nearby molecules of the same type. We employed an aggressive grouping algorithm to address this issue, but the tradeoff is that true separate molecules may be missed. We labeled our own secondary antibodies to control the dye:antibody ratio at ~1:1 to limit multiple blinking, but the labeling creates a distribution and some antibodies will still have multiple fluorophores. Antibodies engineered to have consistent labeling stoichiometry would be an improvement. A trade-off to limiting the dye:antibody ratio is that many of the secondary antibodies will have no fluorophore, reducing labeling efficiency. SMLM techniques generally have shown a labeling efficiency of at most 60% (Feher *et al.*, 2019), which means that rare binding interactions may be hard to detect.

A third challenge for SMLM comes from drift. Autocorrelation drift correction is standard, but it is optimal for defined structures that can be aligned from repeated blinks that occur throughout the acquisition. Singular soluble proteins, which blink only within a small window, pose a challenge for this correction method, and too few blinks overall can prevent the algorithm from working despite apparent drift by eye. Further, this correction method cannot remove high-frequency variation in position through vibration within the microscope. Fluorescent beads may be used as a fiducial marker at the coverglass surface, but a solution is needed that would work throughout the cell. A sparsely labeled ubiquitous cellular structure, like tubulin, could serve this purpose with an appropriately engineered label.

Combined, the improvements discussed above would greatly increase the effective analytical resolution for detection of binding events *in vivo*. Our cross-nearest neighbor/Monte Carlo analytical approach could easily be extended to 3-dimensional STORM data and multi-protein

complexes with three-color STORM. However, care would need to be taken to avoid crosstalk between adjacent fluorescence channels as it would generate false positives.

Previously, we found that MEG3 induces p53 stabilization and stimulates p53-dependent transcription activation (Zhou *et al.*, 2007). We also observed that p53 activated by MEG3 selectively upregulates GDF15, but not p21<sup>CIP1</sup> (Zhou *et al.*, 2007). In this study, we demonstrated that MEG3 lncRNA interacts with p53 in vivo and can be detected with a novel analytical method using dSTORM. We also demonstrated that the p53–Mdm2 interaction is not disrupted by MEG3 in vivo. Taken together, these data suggest that MEG3 activates p53 by an alternative mechanism that is yet to be determined. Finally, we believe our in vivo binding analysis provides a powerful new tool to assess macromolecular interactions in a native cellular context.

## MATERIALS AND METHODS

### Cell lines, media, and growth conditions

The U2OS osteosarcoma cells (ATCC HTB-96) were maintained in Dulbecco's modified Eagle's medium (DMEM) (Gibco 11995065) supplemented with 10% heat-inactivated FBS (Gibco A3060502), glutamine (2 mM), penicillin (100 U/mL), and streptomycin (0.1 mg/mL) (Gibco 10378016) at 37 °C and 10% CO<sub>2</sub>. Doxycycline (Dox; 1 µg/mL) was added to media for at least 20 h to induce expression of the transfected tetracycline-inducible *MEG3*. Nutlin-3a (Nut; 10 µM) was added to media for at least 24 h to inhibit Mdm2-mediated degradation of p53. For microscopy, 3–5×10<sup>4</sup> cells were seeded into each well of a chambered 8-well 1.5H coverglass (Ibidi 80827) and allowed to adhere overnight prior to further manipulation. Cells were tested for mycoplasma contamination every three months. U2OS-MEG3 cells were regularly authenticated by qRT-PCR and/or FISH for induction of MEG3 by doxycycline.

## Plasmid construction and transfection

A modified Tet-On expression system was used to express MEG3, consisting of pBiTetO-MEG3-GFP<sub>LoxP</sub> and pCMV-rtTA3-IRES<sub>puro</sub>. pBiTetO was constructed by replacing the CMV promoter in expression vector pCI with a tetracycline-responsive bi-directional promoter, BiTetO, which was synthesized to contain 7 modified TetO elements flanked by two minimal CMV promoter sequences based on pTet-T2 sequences (GenScript) (Loew *et al.*, 2010). To facilitate selection of clones, a GFP cDNA in with the coding region flanked by two LoxP sites was cloned into pBiTetO to generate pBiTetO-GFP<sub>LoxP</sub>. The MEG3 cDNA in pCI-MEG3 (Zhou *et al.*, 2007) was modified by replacing AATAAA and its downstream poly(A) tail with a genomic DNA fragment containing the MEG3 gene polyadenylation signal. The resultant MEG3 cDNA was then cloned into pBiTetO-GFP<sub>LoxP</sub> to generate pBiTetO-MEG3-GFP<sub>LoxP</sub>. To construct pCMV-rtTA3-IRES<sub>puro</sub>, a modified tetracycline responsive transactivator (rtTA3) was synthesized with changes in three amino acids including F67S, F86Y, and A209T (Das *et al.*, 2004; Zhou *et al.*, 2007) and inserted into pIRES<sub>puro</sub>3 (Clontech Laboratories). Plasmids were verified by sequencing.

For stable transfection, U2OS cells were seeded into 6-well cell culture plates and transfected with pBiTetO-MEG3-GFP<sub>LoxP</sub> and pCMV-rtTA3-IRES<sub>puro</sub> at a ratio of 3 to 1 using Mirus TransIT-LT1 according to the manufacture's instruction. Forty-eight hours after transfection, cells were re-seeded in P100 dishes with limited dilution. Approximately ten days after treatment with puromycin (2 µg/mL), drug resistant colonies were isolated using cloning rings. Cells from individual clones were treated with or without doxycycline (1 µg/mL) for 24 h. GFP expression was evaluated under a fluorescence microscope. Cells expressing GFP in Dox-treated wells were further examined for MEG3 expression by qRT-PCR. Two sets of primers were used to detect MEG3. The first set detected a fragment near the 5' end of the MEG3 cDNA:



5'-ATTAAGCCCTGACCTTTGCTATGC-3' (forward) and 5'-ATAAGGGTGATGACAGAGTCAG-TCG-3' (reverse); the second set detected the 3' end of the MEG3: 5'-CTTCAGTGTCTGCATGTGGGAAG-3' (forward) and 5'-TGCTTTGGAACCGCATCACAG-3' (reverse). The GAPDH gene was used as an internal reference. The primers for detection of GAPDH were: 5'-GATGACATCAAGAAGGTGGTGAAGC-3' (forward) and 5'-CGTTGTCATACCAGGAAATGAGCTTG-3' (reverse). Cell clones with suitable MEG3 induction were treated with adenoviruses expressing Cre (Ad-Cre) to remove the floxed GFP. Up to three rounds of virus treatments were needed to completely remove GFP. The removal of GFP was confirmed by qRT-PCR with primer set: 5'-CCACAACGTCTATATCATGGCCG-3' (forward) and 5'-GTGCTCAGGTAGTGGTTGTCG-3' (reverse). A total of four clones containing inducible MEG3 were finally obtained and designated as U2OS-MEG3.

## **Direct stochastic optical reconstruction microscopy (dSTORM)**

### *Fixation*

Cells were grown to between 30–90% confluence in chambered coverglass. Cells were rinsed with prewarmed Dulbecco's phosphate-buffered saline with calcium and magnesium (DPBS; Corning) twice using near-simultaneous aspiration and injection of liquid to avoid dehydration. Prewarmed fixation buffer (4% (v/v) paraformaldehyde (Electron Microscopy Sciences), 0.1% (v/v) glutaraldehyde (Electron Microscopy Sciences)) was added and incubated in the dark for 15 min. Fixed cells were rinsed with DPBS. Remaining fixative was quenched with 1% (w/v) sodium borohydride (Sigma-Aldrich) for 7 min. (0.1% is typical, but we have observed better suppression of autofluorescence at 1%.) Cells were further quenched and washed with 50 mM glycine (Bio-Rad) in DPBS (DPBS-G) 3 times for 10 min each. Fixed cells were stored for up to a week in DPBS at 4 °C.

### *Immunofluorescence*

Cells were permeabilized with 0.2% Triton X-100 (*t*-octylphenoxypolyethoxyethanol, Sigma-Aldrich) in DPBS for 10 min and rinsed with DPBS. Cells were blocked with 5% normal donkey serum (EMD Millipore)/0.02% (v/v) Triton X-100 in DPBS for 4 h at room temperature or overnight at 4 °C. Primary antibodies (rabbit anti-p53 [7F5] (Cell Signaling 2527S, Lot 8), mouse anti-Mdm2 [2A10] (Abcam ab16895, Lot GR324625-5)) were applied at 1:1000 and 1:200 dilutions, respectively, in blocking buffer and incubated overnight at 4 °C. Cells were washed with DPBS 6 times for 5 min each. Secondary antibodies (donkey anti-rabbit IgG (Jackson ImmunoResearch) and donkey anti-mouse IgG (Jackson ImmunoResearch)) were labeled as previously described with ATTO 488 (ThermoFisher Scientific) or Alexa Fluor 647 (ThermoFisher Scientific) for a dye ratio of ~1:1 (Schmider *et al.*, 2019). Secondary antibodies were added at 3 µg/mL each in blocking buffer and incubated for 2 h at room temperature in the dark. All subsequent steps were performed in the dark. Cells were washed with DPBS 6 times for 5 min each. Antibody stacks were crosslinked by 4% (v/v) paraformaldehyde in DPBS for 15 min. Remaining fixative was quenched and washed with DPBS-G twice for 5 min each, followed by DPBS twice for 5 min each. Stained cells were stored at 4 °C for up to 2 weeks before imaging.

### *Combined immunofluorescence and fluorescence in situ hybridization (FISH)*

All buffers are RNase-free. Cells were permeabilized with 0.2% Triton X-100 in RNase-free PBS (Corning) for 10 min and rinsed with PBS. No blocking was performed to avoid introducing RNase activity. Primary antibody (rabbit anti-p53, see above) were applied at 1:1000 or 1:200 dilutions, respectively, in PBS and incubated overnight at 4 °C. Cells were washed with PBS 6 times for 5 min each. FISH was performed using buffers and ~20-mer tiled probe sets from Stellaris, according to manufacturer's protocol. In brief, cells were washed with Wash Buffer A 2 times for 3 min. MEG3-Quasar 670 (Stellaris, custom order) or GAPDH-Quasar 570 (Stellaris SMF-2026-1) probe mixture was mixed 1:1000 in Hybridization Buffer and 100 µL was added per

well. Steps from this point forward were conducted in the dark. The chambered coverglass was placed in a pre-warmed humidified chamber (large culture dish with damp paper towels) and incubated at 37 °C for 16 h. Cells were washed 2 times for 15 min each with warm Wash Buffer A in the humidified chamber. Secondary antibodies (donkey anti-rabbit conjugated with ATTO 488, see above) were added at 3 µg/mL each in Wash Buffer A and incubated for 1 h at 37 °C in the humidified chamber. Cells were washed 2 times for 2 min each with Wash Buffer B, then 2 times for 5 min each with PBS.

### *Imaging*

Imaging buffer containing 10 mM cysteamine (2-mercaptoethylamine, MEA; Sigma-Aldrich), 3 U/mL pyranose oxidase from *Coriolus* sp. (Sigma P4234), and 90 U/mL catalase was freshly prepared in STORM buffer. Cysteamine stock solution was previously titrated to pH 8 and aliquots frozen. Precipitate in pyranose oxidase/catalase 100x enzyme stock solution was cleared by centrifugation at over 14,000×g prior to use. STORM buffer was composed of 10% (w/v) glucose, 10 mM sodium chloride, and 50 mM Tris hydrochloride (pH 8.0). We found the pyranose oxidase buffer (first described in (Swoboda *et al.*, 2012)) to be superior to the standard glucose oxidase buffer. This buffer allowed longer imaging times due to minimal pH change, and the enzyme stock lasted several months at 4 °C with no observable decline in imaging quality. 10 mM cysteamine was selected for superior imaging characteristics with different dyes (van de Linde *et al.*, 2011). PBS was replaced with the imaging buffer and the slide was mounted on the stage with type F immersion oil (refractive index = 1.515) on a Nikon Ti2 Eclipse inverted microscope. The microscope was equipped with a 100× 1.49 NA APO-TIRF objective with automatic correction collar and a Nikon NSTORM 5.0 system including 405 nm (20 mW), 488 nm (70 mW), 561 nm (70 mW), and 647 nm (125 mW) lasers, a quadband excitation-emission filter, and a Hamamatsu ORCA Flash4.0 V2 S-CMOS camera. Nikon Elements 5.02 was used for image acquisition. A 10×10 tiled (with 10% overlap) widefield fluorescence image (~790×790 µm<sup>2</sup>) was obtained with

1 s exposure using GFPHQ, TexasRedHYQ, or Cy5HYQ filter cubes, from which random individual cells were selected for dSTORM imaging. At least 11000, 256x256 pixel (160  $\mu\text{m}$ /pixel) frames were collected with 10 ms exposure time at 100% laser power with lasers in highly inclined and laminated optical sheet (HILO) configuration (Tokunaga *et al.*, 2008). Each channel was collected sequentially from longest wavelength the shortest.

## Data analysis

Localizations were identified from STORM image stacks using Nikon Elements 5.0 (NSTORM 4.0), with a peak height threshold of 250. Localization lists were exported as tab-delimited text files.

Localization data was processed with custom code written in the freely available Julia scientific computing language (v1.2) (Bezanson *et al.*, 2017). Localizations identified in the first 100 frames, while fluorophores are being placed into the “off” state, were excluded. Localizations identified in the last 10 frames were also excluded due to artifacts caused by the change in optical configuration. For each image, a grouping algorithm (SI Algorithm 1; Figure S3) was applied to each channel to combine repeated blinking from single fluorophores and localizations that may be associated (e.g., another fluorophore on same secondary antibody, another secondary antibody on the same primary antibody, another primary antibody on a multimer). The first stage of the grouping algorithm iteratively identified local density maxima by searching a 34.2 nm radius and within a temporal window of 500 frames (5.0 s) of each localization for the localizations with the most neighbors, combining those localizations within the radius of the maxima, and repeating until all localizations were assigned to a group. The 34.2 nm radius limit was derived from a simulation of the possible orientation and positions of fluorophores in an antibody stack, to account for possible motion of the antibody stack and multiple fluorophores on the stack. The temporal window was applied to account for longer-scale on/off cycles of the fluorophores, as first described for PALM data (Annibale *et al.*, 2011), and was chosen semi-empirically by testing a

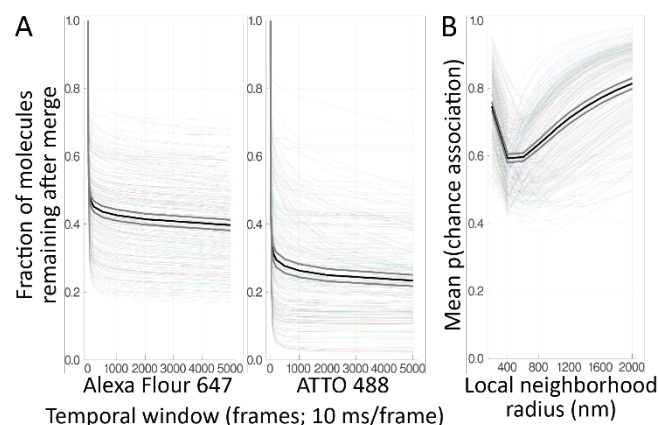


**Figure 7. Analysis of algorithm parameters.** All cells were repeatedly analyzed with the algorithm during development to characterize the effect of parameter choice on outcome. (A,B) Fraction of molecules remaining after grouping, normalized to the number of molecules with size 1, as a function of temporal window size (frames, at 10 ms/frame), for Alexa Fluor 647 and ATTO 488. (B) Mean probability of chance association ( $p(\text{chance association})$ ) as a function of local neighborhood radius (nm). Each faded colored line is from a single cell. Black line shows the mean, gray lines indicate  $\pm 95\%$  confidence interval.

range of values and selecting the smallest value that merged the most localizations (i.e., where the slope starts to decrease before the plateau) (Figure 7A) and where the merge results appeared suitable (e.g., few temporally separated clusters of localizations were merged).

In the second stage, grouped localizations were merged if they were found within 200 nm of each other by a similar local density maxima search algorithm to further reduce redundancy from autocorrelated localizations. The products of this grouping algorithm were termed “molecules.” The position of the resulting molecule was the mean of its component localizations’ positions, and its linear localization accuracy was the mean of the accuracy for its component localizations divided by the square root of the number of component localizations.

The molecules were paired between channels by an exclusive cross-nearest neighbor algorithm (i.e., closest pair found and then removed, next closest pair found and then removed...; SI Algorithm 3) to obtain a distance distribution between the two sets of molecules. Two analytical approaches were applied, simple and sophisticated. First, the median paired distance was calculated for each cell. Second, a novel approach was developed to control for local density, based on a similar approach applied to single-molecule conventional fluorescence microscopy (Eliscovich *et al.*, 2017). Random permutations (10,000) of the molecules in the local (800 nm radius) neighborhood around each potential binding pair were generated and the closest pairwise

distance in each permutation was calculated to create a Monte Carlo estimation of the distribution of distances due to local density (SI Algorithm 4). The local neighborhood radius of 800 nm was semi-empirically chosen based on testing multiple window sizes with the algorithm and choosing the value that provided a balance of sensitivity (smaller value) and robustness (less inter-sample change as parameter changes) (Figure 7B). The fraction of permutations with a closest distance less than the observed distance was the percentile rank score, indicating the probability of chance association given the local density of both molecule types. Finally, the fraction of pairs within the maximum binding distance (200 nm) and with a probability of chance association of less than 0.1 was calculated for each cell. The maximum binding distance was chosen based on knowledge of the size of the target molecules (up to 20 nm across) and the size of the antibody stacks (up to 70 nm), with allowance for error. These data were analyzed by two-way fixed-factor ANOVA with 2 nested factors (cells within replicates within conditions), with  $\alpha = 0.05$ , using the SimpleANOVA.jl (v0.6.0) Julia package created by the authors. Data was checked for extreme outliers, heteroscedasticity, and normality of residuals, and were determined to be reasonable. Plots were generated with StatsPlots.jl (v0.12.0) and assembled with Adobe Illustrator 24.0.

### Code availability

All the code generated specifically for this manuscript is written in the Julia language and available in the repository at [https://github.com/BioTurboNick/SMLMAssociationAnalysis\\_NCB.jl](https://github.com/BioTurboNick/SMLMAssociationAnalysis_NCB.jl). Supporting packages can be obtained within Julia from its public package registry.

### ACKNOWLEDGEMENTS

We thank Dr. Angie Schmider and Nikon for training on the STORM system; Dr. Hongjae Sunwoo for advice on combining FISH and STORM; Dr. Carolina Eliscovich for help understanding her Monte Carlo-based method; and Dr. Hang Lee of Harvard Catalyst for

statistical advice. Funding: RJS: R01CA193520, R01DK062472, S10RR027931; NCB: T32DK007540; AK and YZ: R01CA193520; and The Jarislowsky Foundation

## REFERENCES

- Annibale, P., Vanni, S., Scarselli, M., Rothlisberger, U., and Radenovic, A. (2011). Identification of clustering artifacts in photoactivated localization microscopy. *Nat Methods* **8**, 527.
- Bauer, N.C., Doetsch, P.W., and Corbett, A.H. (2015). Mechanisms regulating protein localization. *Traffic* **16**, 1039-1061.
- Bezanson, J., Edelman, A., Karpinski, S., and Shah, V.B. (2017). Julia: a fresh approach to numerical computing. *SIAM Rev* **59**, 65-98.
- Braconi, C., Kogure, T., Valeri, N., Huang, N., Nuovo, G., Costinean, S., Negrini, M., Miotto, E., Croce, C.M., and Patel, T.D. (2011). microRNA-29 can regulate expression of the long non-coding RNA gene *MEG3* in hepatocellular cancer. *Oncogene* **30**, 4750-4756.
- Carrington, G., Tomlinson, D., and Peckham, M. (2019). Exploiting nanobodies and affimers for superresolution imaging in light microscopy. *Mol Biol Cell* **30**, 2737-2740.
- Cheunsuchon, P., Zhou, Y., Zhang, X., Lee, H., Chen, W., Nakayama, Y., Rice, K.A., Tessa Hedley-Whyte, E., Swearingen, B., and Klibanski, A. (2011). Silencing of the imprinted *DLK1-MEG3* locus in human clinically nonfunctioning pituitary adenomas. *Am J Pathol* **179**, 2120-2130.
- Das, A.T., Zhou, X., Vink, M., Klaver, B., Verhoef, K., Marzio, G., and Berkhout, B. (2004). Viral evolution as a tool to improve the tetracycline-regulated gene expression system. *J Biol Chem* **279**, 18776-18782.
- Das, P.P., Hendrix, D.A., Apostolou, E., Buchner, A.H., Canver, M.C., Beyaz, S., Ljuboja, D., Kuintzle, R., Kim, W., Karnik, R., et al. (2015). PRC2 is required to maintain expression of the maternal *Gtl2-Rian-Mirg* locus by preventing de novo DNA methylation in mouse embryonic stem cells. *Cell Rep* **12**, 1456-1470.



- Eliscovich, C., Shenoy, S.M., and Singer, R.H. (2017). Imaging mRNA and protein interactions within neurons. *Proc Natl Acad Sci U S A* 114, E1875-e1884.
- Feher, K., Halstead, J.M., Goyette, J., and Gaus, K. (2019). Can single molecule localization microscopy detect nanoclusters in T cells? *Curr Opin Chem Biol* 51, 130-137.
- Gejman, R., Batista, D.L., Zhong, Y., Zhou, Y., Zhang, X., Swearingen, B., Stratakis, C.A., Hedley-Whyte, E.T., and Klibanski, A.D. (2008). Selective loss of *MEG3* expression and intergenic differentially methylated region hypermethylation in the *MEG3/DLK1* locus in human clinically nonfunctioning pituitary adenomas. *J Clin Endocrinol Metab* 93, 4119-4125.
- Gu, J., Kawai, H., Nie, L., Kitao, H., Wiederschain, D., Jochemsen, A.G., Parant, J., Lozano, G., and Yuan, Z.M. (2002). Mutual dependence of MDM2 and MDMX in their functional inactivation of p53. *J Biol Chem* 277, 19251-19254.
- Huang, L., Yan, Z., Liao, X., Li, Y., Yang, J., Wang, Z.G., Zuo, Y., Kawai, H., Shadfan, M., Ganapathy, S., et al. (2011). The p53 inhibitors MDM2/MDMX complex is required for control of p53 activity in vivo. *Proc Natl Acad Sci U S A* 108, 12001-12006.
- Jia, L.F., Wei, S.B., Gan, Y.H., Guo, Y., Gong, K., Mitchelson, K., Cheng, J., and Yu, G.Y. (2014). Expression, regulation and roles of miR-26a and MEG3 in tongue squamous cell carcinoma. *Int J Cancer* 135, 2282-2293.
- Kaneko, S., Bonasio, R., Saldana-Meyer, R., Yoshida, T., Son, J., Nishino, K., Umezawa, A., and Reinberg, D. (2014). Interactions between JARID2 and noncoding RNAs regulate PRC2 recruitment to chromatin. *Mol Cell* 53, 290-300.
- Li, L., Tao, Q., Jin, H., van Hasselt, A., Poon, F.F., Wang, X., Zeng, M.-S., Jia, W.-H., Zeng, Y.-X., Chan, A.T.C., et al. (2010). The tumor suppressor UCHL1 forms a complex with p53/MDM2/ARF to promote p53 signaling and is frequently silenced in nasopharyngeal carcinoma. *Clin Cancer Res* 16, 2949-2958.

- Li, R., Fang, L., Pu, Q., Bu, H., Zhu, P., Chen, Z., Yu, M., Li, X., Weiland, T., Bansal, A., et al. (2018). MEG3-4 is a miRNA decoy that regulates IL-1 $\beta$  abundance to initiate and then limit inflammation to prevent sepsis during lung infection. *Sci Signal* 11.
- Linares, L.K., Hengstermann, A., Ciechanover, A., Muller, S., and Scheffner, M. (2003). HdmX stimulates Hdm2-mediated ubiquitination and degradation of p53. *Proc Natl Acad Sci U S A* 100, 12009-12014.
- Loew, R., Heinz, N., Hampf, M., Bujard, H., and Gossen, M. (2010). Improved Tet-responsive promoters with minimized background expression. *BMC Biotechnol* 10, 81.
- Lu, K.H., Li, W., Liu, X.H., Sun, M., Zhang, M.L., Wu, W.Q., Xie, W.P., and Hou, Y.D. (2013). Long non-coding RNA MEG3 inhibits NSCLC cells proliferation and induces apoptosis by affecting p53 expression. *BMC Cancer* 13, 461.
- Mondal, T., Subhash, S., Vaid, R., Enroth, S., Uday, S., Reinius, B., Mitra, S., Mohammed, A., James, A.R., Hoberg, E., et al. (2015). MEG3 long noncoding RNA regulates the TGF-beta pathway genes through formation of RNA-DNA triplex structures. *Nat Commun* 6, 7743.
- Naoki, M., Hirotaka, W., Shigeharu, W., Toshihiko, S., Masashi, N., Kohzoh, A., Takashi, K., Azim, S.M., Tomoko, K.I., and Fumitoshi, I. (2000). Identification of an imprinted gene, *Meg3/Gtl2* and its human homologue *MEG3*, first mapped on mouse distal chromosome 12 and human chromosome 14q. *Genes Cells* 5, 211-220.
- Perry, M.E. (2010). The regulation of the p53-mediated stress response by MDM2 and MDM4. *Cold Spring Harb Perspect Biol* 2, a000968.
- Qu, C., Jiang, T., Li, Y., Wang, X., Cao, H., Xu, H., Qu, J., and Chen, J.G. (2013). Gene expression and IG-DMR hypomethylation of maternally expressed gene 3 in developing corticospinal neurons. *Gene Expr Patterns* 13, 51-56.
- Riley, K.J., and Maher, L.J., 3rd. (2007). p53 RNA interactions: new clues in an old mystery. *RNA* 13, 1825-1833.

- Ryan, K.M., Phillips, A.C., and Vousden, K.H. (2001). Regulation and function of the p53 tumor suppressor protein. *Curr Opin Cell Biol* 13, 332-337.
- Saphire, E.O., Stanfield, R.L., Crispin, M.D., Parren, P.W., Rudd, P.M., Dwek, R.A., Burton, D.R., and Wilson, I.A. (2002). Contrasting IgG structures reveal extreme asymmetry and flexibility. *J Mol Biol* 319, 9-18.
- Savchenko, A., Yurchenko, M., Snopok, B., and Kashuba, E. (2008). Study on the spatial architecture of p53, MDM2, and p14ARF containing complexes. *Mol Biotechnol* 41, 270.
- Schmider, A.B., Vaught, M., Bauer, N.C., Elliott, H.L., Godin, M.D., Ellis, G.E., Nigrovic, P.A., and Soberman, R.J. (2019). The organization of leukotriene biosynthesis on the nuclear envelope revealed by single molecule localization microscopy and computational analyses. *PLoS One* 14, e0211943.
- Sheng, X., Li, J., Yang, L., Chen, Z., Zhao, Q., Tan, L., Zhou, Y., and Li, J.D. (2014). Promoter hypermethylation influences the suppressive role of maternally expressed 3, a long non-coding RNA, in the development of epithelial ovarian cancer. *Oncology reports* 32, 277-285.
- Sloan, K.E., Bohnsack, M.T., and Watkins, N.J. (2013). The 5S RNP couples p53 homeostasis to ribosome biogenesis and nucleolar stress. *Cell Rep* 5, 237-247.
- Sograte-Idrissi, S., Oleksiievets, N., Isbaner, S., Eggert-Martinez, M., Enderlein, J., Tsukanov, R., and Opazo, F. (2019). Nanobody detection of standard fluorescent proteins enables multi-target DNA-PAINT with high resolution and minimal displacement errors. *Cells* 8.
- Sun, M., Xia, R., Jin, F., Xu, T., Liu, Z., De, W., and Liu, X.D. (2014). Downregulated long noncoding RNA MEG3 is associated with poor prognosis and promotes cell proliferation in gastric cancer. *Tumour Biol* 35, 1065-1073.
- Swoboda, M., Henig, J., Cheng, H.M., Brugger, D., Haltrich, D., Plumere, N., and Schlierf, M. (2012). Enzymatic oxygen scavenging for photostability without pH drop in single-molecule experiments. *ACS Nano* 6, 6364-6369.

- Takahashi, N., Kobayashi, R., and Kono, T.D. (2010). Restoration of *Dlk1* and *Rtl1* is necessary but insufficient to rescue lethality in intergenic differentially methylated region (IG-DMR)-deficient mice. *J Biol Chem* 285, 26121-26125.
- Takahashi, N., Okamoto, A., Kobayashi, R., Shirai, M., Obata, Y., Ogawa, H., Sotomaru, Y., and Kono, T.D. (2009). Deletion of *Gtl2*, imprinted non-coding RNA, with its differentially methylated region induces lethal parent-origin-dependent defects in mice. *Human Mol Genet* 18, 1879-1888.
- Tokunaga, M., Imamoto, N., and Sakata-Sogawa, K. (2008). Highly inclined thin illumination enables clear single-molecule imaging in cells. *Nat Methods* 5, 159-161.
- Toledo, F., and Wahl, G.M. (2006). Regulating the p53 pathway: in vitro hypotheses, in vivo veritas. *Nat Rev Cancer* 6, 909-923.
- Uroda, T., Anastasakou, E., Rossi, A., Teulon, J.M., Pellequer, J.L., Annibale, P., Pessey, O., Inga, A., Chillon, I., and Marcia, M. (2019). Conserved pseudoknots in lncRNA MEG3 are essential for stimulation of the p53 pathway. *Mol Cell* 75, 982-995.e989.
- van de Linde, S., Loschberger, A., Klein, T., Heidbreder, M., Wolter, S., Heilemann, M., and Sauer, M. (2011). Direct stochastic optical reconstruction microscopy with standard fluorescent probes. *Nat Protoc* 6, 991-1009.
- Wang, P., Ren, Z., and Sun, P. (2012). Overexpression of the long non-coding RNA MEG3 impairs in vitro glioma cell proliferation. *J Cell Biochem* 113, 1868-1874.
- Yan, H., Yuan, J., Gao, L., Rao, J., and Hu, J. (2016). Long noncoding RNA MEG3 activation of p53 mediates ischemic neuronal death in stroke. *Neuroscience* 337, 191-199.
- Yan, J., Guo, X., Xia, J., Shan, T., Gu, C., Liang, Z., Zhao, W., and Jin, S.D. (2014). MiR-148a regulates MEG3 in gastric cancer by targeting DNA methyltransferase 1. *Med Oncol* 31, 879.
- Zacchi, P., Gostissa, M., Uchida, T., Salvagno, C., Avolio, F., Volinia, S., Ronai, Z., Blandino, G., Schneider, C., and Del Sal, G. (2002). The prolyl isomerase Pin1 reveals a mechanism to control p53 functions after genotoxic insults. *Nature* 419, 853-857.

- Zhang, X., Gejman, R., Mahta, A., Zhong, Y., Rice, K.A., Zhou, Y., Cheunsuchon, P., Louis, D.N., and Klibanski, A.D. (2010). Maternally expressed gene 3, an imprinted noncoding RNA gene, is associated with meningioma pathogenesis and progression. *Cancer Res* 70, 2350-2358.
- Zhang, X., Zhou, Y., Mehta, K.R., Danila, D.C., Scolavino, S., Johnson, S.R., and Klibanski, A. (2003). A pituitary-derived MEG3 isoform functions as a growth suppressor in tumor cells. *J Clin Endocrinol Metab* 88, 5119-5126.
- Zhao, J., Dahle, D., Zhou, Y., Zhang, X., and Klibanski, A.D. (2005). Hypermethylation of the promoter region is associated with the loss of MEG3 gene expression in human pituitary tumors. *J Clin Endocrinol Metab* 90, 2179-2186.
- Zhao, J., Ohsumi, T.K., Kung, J.T., Ogawa, Y., Grau, D.J., Sarma, K., Song, J.J., Kingston, R.E., Borowsky, M., and Lee, J.T. (2010). Genome-wide identification of polycomb-associated RNAs by RIP-seq. *Mol Cell* 40, 939-953.
- Zheng, H., You, H., Zhou, X.Z., Murray, S.A., Uchida, T., Wulf, G., Gu, L., Tang, X., Lu, K.P., and Xiao, Z.X. (2002). The prolyl isomerase Pin1 is a regulator of p53 in genotoxic response. *Nature* 419, 849-853.
- Zhou, Y., Zhong, Y., Wang, Y., Zhang, X., Batista, D.L., Gejman, R., Ansell, P.J., Zhao, J., Weng, C., and Klibanski, A.D. (2007). Activation of p53 by MEG3 non-coding RNA. *J Biol Chem* 282, 24731-24742.
- Zhu, J., Liu, S., Ye, F., Shen, Y., Tie, Y., Zhu, J., Wei, L., Jin, Y., Fu, H., Wu, Y., et al. (2015). Long noncoding RNA MEG3 interacts with p53 protein and regulates partial p53 target genes in hepatoma cells. *PloS One* 10, e0139790.